[Research Paper] 대한금속 · 재료학회지 (*Korean J. Met. Mater.*), Vol. 61, No. 1 (2023) pp.46-53
DOI: 10.3365/KJMM.2023.61.1.46

Enhanced Thermoelectric Performance of Sn-Doped Permingeatites $Cu_3Sb_{1-y}Sn_ySe_4$

Ji-Hee Pi, Go-Eun Lee, and Il-Ho Kim*

Department of Materials Science and Engineering, Korea National University of Transportation, Chungju 27469, Republic of Korea

Abstract: In this study, $Cu_3Sb_{1-y}Sn_ySe_4$ ($0 \le y \le 0.08$) permingeatites were synthesized via mechanical alloying followed by hot pressing. The phase transformation, microstructure, charge transport parameters of the permingeatites, and their thermoelectric properties were analyzed. The permingeatites were present in a single phase with a tetragonal structure, and secondary phases were not detected. The permingeatites had relative densities of 97.2%–98.5%. The lattice constants of the a- and c-axis increased when Sn was substituted at the Sb sites. With increasing Sn content, the carrier concentration increased to (2.2–4.1) × 10^{19} cm^{-3}; however, mobility did not change significantly, at 58–66 $cm^2V^{-1}s^{-1}$. The undoped Cu_3SbSe_4 behaved as a non-degenerate semiconductor. Its Lorenz number was calculated to be (1.57–1.56) × 10^{-8} V^2K^{-2} at 323–623 K, and a maximum dimensionless figure of merit (*ZT*) of 0.39 was obtained at the temperature of 623 K, power factor of 0.49 $mWm^{-1}K^{-2}$, and thermal conductivity of 0.76 $Wm^{-1}K^{-1}$. However, the Sn-doped specimens behaved as degenerate semiconductors. Their Lorenz numbers increased to (1.63–1.94) × 10^{-8} V^2K^{-2} at 323–623 K. $Cu_3Sb_{0.96}Sn_{0.04}Se_4$ exhibited a remarkably enhanced *ZT* of 0.71 at a temperature of 623 K, power factor of 1.18 $mWm^{-1}K^{-2}$, and thermal conductivity of 1.01 $Wm^{-1}K^{-1}$.

(Received 4 October, 2022; Accepted 31 October, 2022)

Keywords: permingeatite, thermoelectric, charge transport

1. INTRODUCTION

The ongoing development of eco-friendly and cost-effective thermoelectric materials has recently attracted increasing attention [1,2]. Several interesting candidates with promising electrochemical properties have been identified from the Cu-Sb-Se ternary chalcogenides. One such candidate, permingeatite (Cu_3SbSe_4), belongs to the tetragonal crystal structure with the space group $I\bar{4}2m$ [3-5].

A unit cell of Cu_3SbSe_4 contains four times more atoms than that of ZnSe [6]. Cu_3SbSe_4 has a crystal structure comprised of one-dimensional Sb-Se arrays of inserted $SbSe_4$ tetrahedrons and three-dimensional Cu-Se frameworks of distorted $CuSe_4$ tetrahedrons [5]. The Sb-Se bond lengths are greater than the Cu-Se bond lengths, and the Cu^{I}-Se bond lengths are different than the Cu^{II}-Se bond lengths. These bonding differences increase the anisotropy of phonon scattering and charge transport and affect the thermal and electrical properties of the material [5]. Cu_3SbSe_4 has been considered as a promising thermoelectric material because of its large carrier effective mass (~1.1 m_o) and narrow direct bandgap (0.13–0.42 eV) [3,6]. Nevertheless, to become a viable thermoelectric material, systematic doping studies need to be conducted to address its high electrical resistivity and high thermal conductivity [3].

The effect of dopants on the thermoelectric performance of permingeatite has been investigated in previous studies. For example, Zhao et al. [7] obtained a *ZT* of 0.54 at 650 K for $Cu_3Sb_{0.985}Ga_{0.015}Se_4$, whereas Li et al. [8] reported a *ZT* of 0.58 at 600 K for $Cu_3Sb_{0.97}Al_{0.03}Se_4$. Furthermore, Chang et al. [9] reported a *ZT* of 0.7 at 640 K for $Cu_3Sb_{0.96}Ge_{0.04}Se_4$, while Li et al. [10] reported a *ZT* of 0.7 at 600 K for $Cu_3Sb_{0.98}Bi_{0.02}Se_4$.

Because the ionic radius of Sn^{4+} (69 pm) is similar to that of Sb^{5+} (60 pm) and because Sn contains one less valence electron than Sb, it is reasonable to assume that Sn is a great acceptor for Cu_3SbSe_4; previously reported studies have confirmed this notion. For example, Wu et al. [11] synthesized $Cu_3Sb_{0.98}Sn_{0.02}Se_4$ by a wet chemical reaction using organic precursors and a hot pressing (HP) method, and

- 피지희 · 이고은: 박사과정, 김일호: 교수
*Corresponding Author: Il-Ho Kim
[Tel: +82-10-5338-1582, E-mail: ihkim@ut.ac.kr]

reported a *ZT* of 0.48 at 575 K. Yang et al. [5] prepared $Cu_3Sb_{0.975}Sn_{0.025}Se_4$ by encapsulated melting (at 773 K for 24 h) and annealing (at 723 K for 24 h), and reported a *ZT* of 0.75 at 730 K. Li et al. [12] synthesized $Cu_3Sb_{0.98}Sn_{0.02}Se_4$ by co-precipitation and HP, and reported a *ZT* of 1.05 at 690 K. Bhardwaj et al. [13] prepared $Cu_3Sb_{0.985}Sn_{0.015}Se_4$ by encapsulated melting (at 773 K for 148 h) and spark plasma sintering, and reported a *ZT* of 1.1 at 623 K. Prasad et al. [14] prepared $Cu_3Sb_{0.98}Sn_{0.02}Se_4$ by annealing (at 723 K for 96 h) pellets made of pressed powder, and reported a *ZT* of 0.12 at 374 K. Finally, Wei et al. [15] synthesized $Cu_3Sb_{0.98}Sn_{0.02}Se_4$ by mechanical alloying (MA) at 450 rpm for 10 h under Ar/N_2 atmosphere and spark plasma sintering, and reported a *ZT* of 0.70 at 673 K.

In our previous study [16], we successfully prepared an undoped permingeatite (Cu_3SbSe_4) via a solid-state synthesis consisting of MA (350 rpm, 12 h) and HP (573 K; 2 h and 70 MPa). Because the synthesized Cu_3SbSe_4 exhibited a low *ZT* of 0.39 at 623 K, we examined the B^{IV}-group elements, such as $_{14}$Si, $_{32}$Ge, and $_{50}$Sn, to determine a suitable dopant to improve its thermoelectric performance. In this study, Sn-doped permingeatites $Cu_3Sb_{1-y}Sn_ySe_4$ ($0 \le y \le 0.08$) were synthesized via MA-HP processes, and their thermoelectric properties were evaluated.

2. EXPERIMENTAL PROCEDURE

To synthesize $Cu_3Sb_{1-y}Sn_ySe_4$ (y = 0, 0.02, 0.04, 0.06, and 0.08), we first stoichiometrically weighed powders of Cu (purity 99.9%, < 45 μm, Kojundo), Sb (purity 99.999%, < 150 μm, Kojundo), Sn (purity 99.999%, < 35 μm, LTS), and Se (purity 99.9%, < 10 μm, Kojundo). The MA process consisted of grinding these powders together in a planetary ball mill (Fritsch, Pulverisette 5). The mixed powders were then sintered by HP using a graphite die. The MA-HP process conditions for permingeatite synthesis have been previously reported [16].

Phases were analyzed by X-ray diffraction (XRD; Bruker, D8-Advance) with Cu Kα. Diffraction peaks and angles were measured for 2θ = 10–90° at a scanning step of 0.02° and scanning speed of 0.4 s/step. Lattice constants were calculated via Rietveld refinement (using the TOPAS software). The microstructure of the specimens was observed by scanning electron microscopy (SEM; FEI, Quanta400) using the backscattered electron (BSE) mode. Elemental line scans and maps were analyzed by energy dispersive spectrometry (EDS; Bruker, XFlash4010) using the following energy levels: Cu *K*-series, Sb *L*-series, Sn *L*-series, and Se *K*-series. Charge transport parameters were estimated by measuring the Hall effect using the van der Pauw method (Keithley 7065). Thermoelectric properties were examined at temperatures from 323 to 623 K. Thermal conductivity was calculated from specific heat, density, and thermal diffusivity measured by TC-9000H (Advance Riko) equipment using the laser flash method. Electrical conductivity and Seebeck coefficient were simultaneously measured using a ZEM-3 (Advance Riko) system with the four-probe method. Finally, the power factor and *ZT* were also calculated.

3. RESULTS AND DISCUSSION

Figure 1 presents the XRD patterns of the Sn-doped permingeatite $Cu_3Sb_{1-y}Sn_ySe_4$. All the diffraction peaks match the standard diffraction pattern for permingeatites (ICDD PDF# 01-085-0003). This confirms the existence of only a single phase with a tetragonal structure. Wu et al. [11], Li et al. [12], and Bhardwaj et al. [13] reported that diffraction peaks of permingeatites without secondary phases were not significantly influenced by low levels of Sn doping

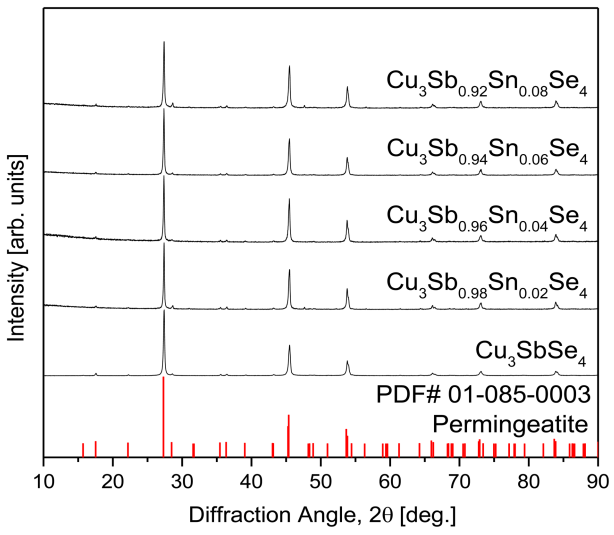

Fig. 1. XRD patterns of $Cu_3Sb_{1-y}Sn_ySe_4$ permingeatite compounds.

Table 1. Chemical compositions, relative densities, and lattice constants of $Cu_3Sb_{1-y}Sn_ySe_4$.

Composition		Relative density	Lattice constant [nm]	
Nominal	Actual	[%]	*a*-axis	*c*-axis
Cu_3SbSe_4	$Cu_{3.44}Sb_{0.67}Se_{3.89}$	98.1	0.56488	1.12434
$Cu_3Sb_{0.98}Sn_{0.02}Se_4$	$Cu_{2.91}Sb_{0.84}Sn_{0.05}Se_{4.21}$	98.4	0.56501	1.12468
$Cu_3Sb_{0.96}Sn_{0.04}Se_4$	$Cu_{2.99}Sb_{0.82}Sn_{0.06}Se_{4.13}$	98.3	0.56507	1.12477
$Cu_3Sb_{0.94}Sn_{0.06}Se_4$	$Cu_{2.93}Sb_{0.76}Sn_{0.06}Se_{4.24}$	97.2	0.56512	1.12520
$Cu_3Sb_{0.92}Sn_{0.08}Se_4$	$Cu_{2.89}Sb_{0.76}Sn_{0.08}Se_{4.26}$	98.5	0.56525	1.12520

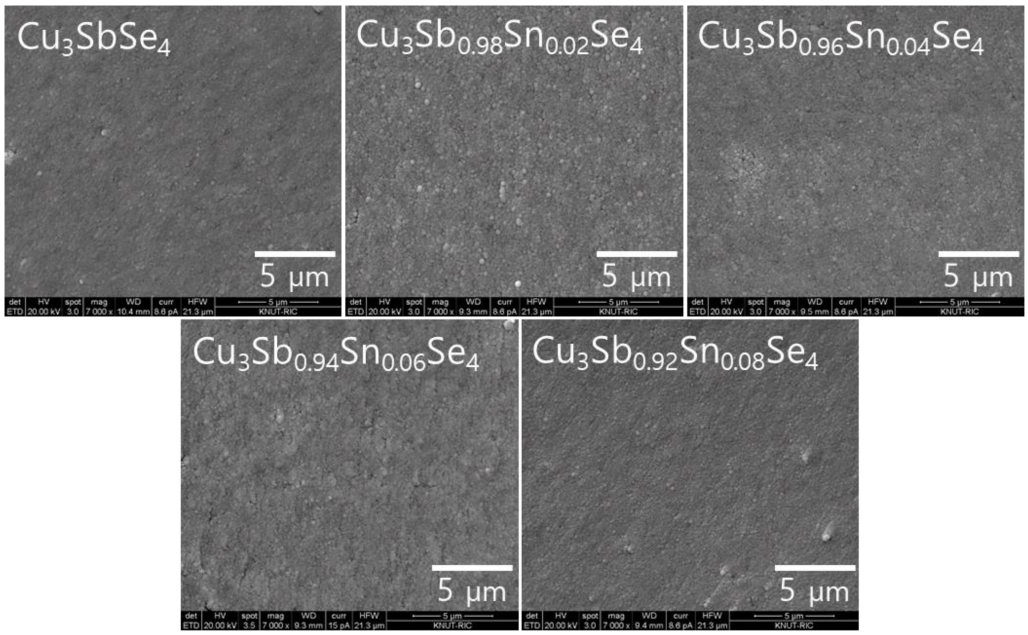

Fig. 2. SEM images of the fractured surfaces of hot-pressed $Cu_3Sb_{1-y}Sn_ySe_4$.

($y \leq 0.02$) at the Sb sites. In contrast, in the proposed study, the diffraction peaks shifted to lower angles as a result of doping with Sn ($y \leq 0.08$). The lower angles indicate lattice expansion. The calculated lattice constants are summarized in Table 1. As the Sn doping increased, *a*- and *c*-axis increased from 0.56488 to 0.56525 nm and 1.12434 to 1.12520 nm, respectively. This confirms that Sn was successfully substituted at the Sb sites. Yang et al. [5] reported that *a*- and *c*-axis of $Cu_3Sb_{1-y}Sn_ySe_4$ (y = 0, 0.025, and 0.05) increased with increasing Sn content, and the lattice expanded because the ionic radius of Sn^{4+} (69 pm) is larger than that of Sb^{5+} (60 pm).

Figure 2 shows the fractured surfaces (SEM images) of our synthesized $Cu_3Sb_{1-y}Sn_ySe_4$ samples. As shown in Table 1, the samples have relative densities of 97.2%–98.5% compared to the theoretical density (5.82 gcm^{-3}) for permingeatites [17]. Secondary phases were not observed, and microstructure did not change significantly with an increase in the Sn content.

Figure 3 presents the BSE-SEM image with EDS line scans and maps of $Cu_3Sb_{0.96}Sn_{0.04}Se_4$. The matrix is a single permingeatite phase without secondary phases, which is consistent with the XRD results shown in Figure 1. Each constituent element is homogeneously distributed, and the elemental line scans and maps confirm the uniform distribution of the low Sn content. The actual compositions are similar to their corresponding nominal compositions, as shown in Table 1. However, given the low levels of Sn involved, there is a possibility of analysis error for this data.

Figure 4 shows the charge transport parameters of $Cu_3Sb_{1-y}Sn_ySe_4$. As can be observed, as the Sn content increased, the carrier concentration increased, but mobility did not vary significantly. Specifically, the carrier concentration and mobility of intrinsic Cu_3SbSe_4 were 5.2×10^{18} cm^{-3} and 50

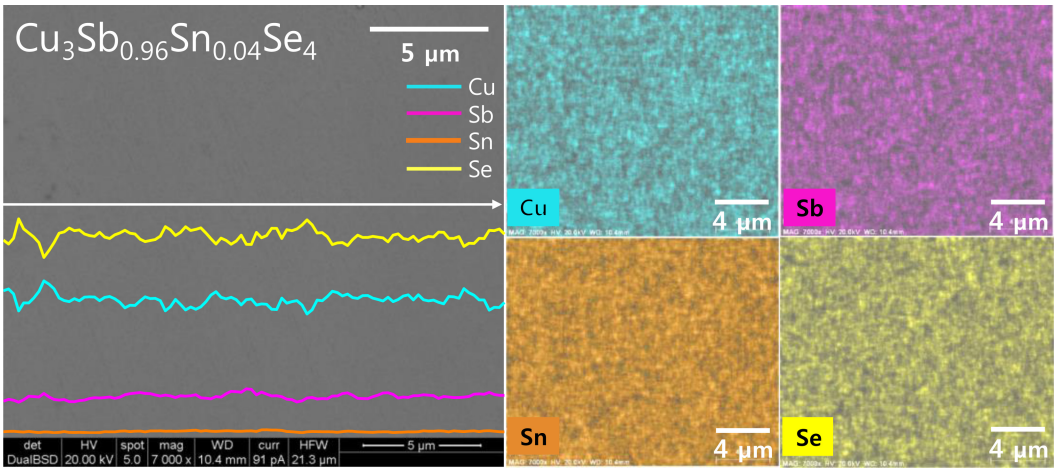

Fig. 3. BSE-SEM micrograph with EDS line scans and elemental maps of $Cu_3Sb_{0.96}Sn_{0.04}Se_4$.

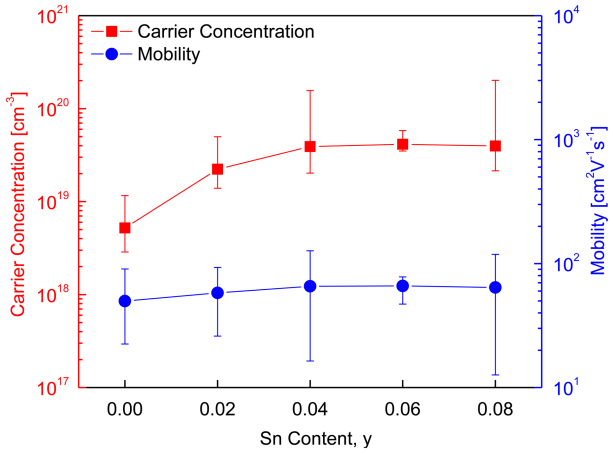

Fig. 4. Carrier concentration and mobility of $Cu_3Sb_{1-y}Sn_ySe_4$.

$cm^2V^{-1}s^{-1}$, respectively, whereas those of the Sn-doped specimens (y = 0.02–0.08) increased to (2.2–4.1) × 10^{19} cm^{-3} and 58–66 $cm^2V^{-1}s^{-1}$, respectively. Studies based on the carrier concentration and mobility of doped Cu_3SbSe_4 have been reported previously. For example, Yang et al. [5] reported a carrier concentration of 7.5 × 10^{18} cm^{-3} and mobility of 41 $cm^2V^{-1}s^{-1}$ for Cu_3SbSe_4, but Sn-doped specimens (y = 0.025–0.05) showed a significantly increased carrier concentration of (6.3–7.8) × 10^{19} cm^{-3} and slightly decreased mobility of 35–31 $cm^2V^{-1}s^{-1}$. The slight decrease in mobility was attributed to the increased electron scattering induced by lattice distortion and ionized scattering centers.

Similarly, Wei et al. [15] reported that Sn doping (y = 0.01–0.04) on Cu_3SbSe_4 increased the carrier concentration from 5.0 × 10^{19} to 2.1 × 10^{20} cm^{-3}, but reduced mobility from 45 to 35 $cm^2V^{-1}s^{-1}$ because of acoustic phonon scattering. Brooks et al. [18] suggested that for non-degenerate semiconductors, mobility decreases with an increase in carrier concentration; this contradicts the findings of our study, where an increase in Sn doping was associated with an increase in carrier concentration, as well as a slight increase in mobility.

Figure 4 also shows that the measured Hall coefficients lie within the acceptable error range and that the Sn doping causes a transition in the samples from non-degenerate semiconductor to degenerate semiconductor. Suzumura et al. [19] explained that both carrier concentration and mobility could be increased by doping with degenerate semiconductors. In addition, Eum et al. [20] reported that although carrier concentration was increased by the substitution of Se at the Te sites on Bi_2Te_3, mobility could also increase because of the reduction in the charge carriers' interface scattering. In such cases, the reduction in scattering can be attributed to the grain growth caused by the HP process.

Figure 5 shows the electrical conductivity of $Cu_3Sb_{1-y}Sn_ySe_4$. With increasing temperature, the electrical conductivity of Cu_3SbSe_4 increased slightly, exhibiting non-degenerate semiconductor behavior. At a constant temperature, the electrical conductivity of the Sn-doped samples increased with increased doping levels. However, as temperature increased, the electrical conductivity of the Sn-doped samples decreased slightly, exhibiting degenerate semiconductor behavior.

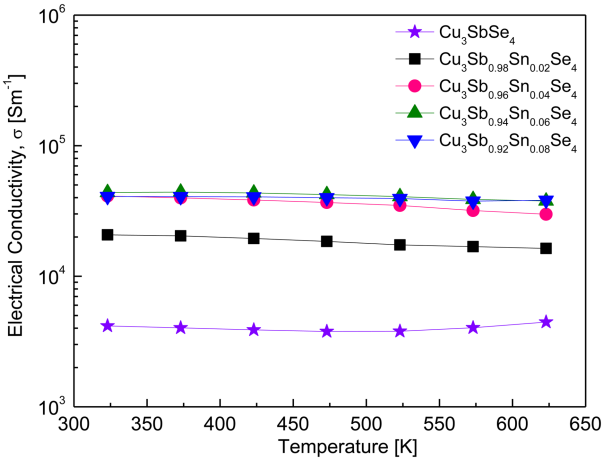

Fig. 5. Temperature dependence of electrical conductivity of $Cu_3Sb_{1-y}Sn_ySe_4$.

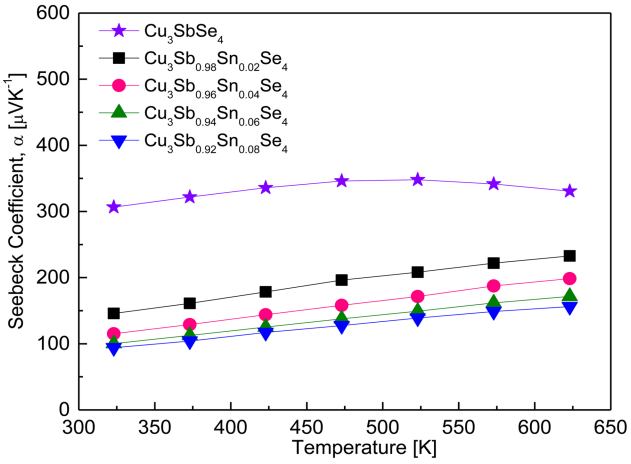

Fig. 6. Temperature dependence of the Seebeck coefficient of $Cu_3Sb_{1-y}Sn_ySe_4$.

Specifically, in our study, the electrical conductivity of Cu_3SbSe_4 was (4.2–4.5) × 10^3 Sm^{-1} at 323–623 K. The Sn-doped specimens exhibited significantly increased values of (2.1–4.1) × 10^4 Sm^{-1} at 323 K and (1.6–3.8) × 10^4 Sm^{-1} at 623 K. Yang et al. [5] reported a similar electrical conductivity for Cu_3SbSe_4, which was (4.9–5.2) × 10^3 Sm^{-1} at 323–623 K, as well as an increase in the electrical conductivity of $Cu_3Sb_{1-y}Sn_ySe_4$ ($0.025 \le y \le 0.05$) to (3.4–3.9) × 10^4 Sm^{-1} at 323 K and (2.4–2.6) × 10^4 Sm^{-1} at 623 K. The increase in conductivity was correlated to an increase in carrier concentration, from 7.5 × 10^{18} to 7.8 × 10^{19} cm^{-3} by Sn doping. Similarly, Wu et al. [11] measured a low electrical conductivity for Cu_3SbSe_4 at (1.0–5.0) × 10^3 Sm^{-1} at 300–570 K, while reporting an increase in the electrical conductivity of $Cu_3Sb_{0.98}Sn_{0.02}Se_4$ to (4.4–2.5) × 10^4 Sm^{-1} at the same temperatures. As shown in Figure 4, increased carrier concentration from Sn doping results in an increase in electrical conductivity. This increase in carrier concentration results from the excess carriers (holes) that are generated when Sn^{4+} is substituted for Sb^{5+}.

Figure 6 shows the Seebeck coefficient of the $Cu_3Sb_{1-y}Sn_ySe_4$ samples. All the samples behaved as p-type semiconductors, suggesting that the major carriers are holes, as confirmed by the positive Hall coefficients of the samples. The Seebeck coefficient for Cu_3SbSe_4 increased from 307 μVK^{-1} at 323 K to 348 μVK^{-1} at 523 K, and then decreased to 331 μVK^{-1} at 623 K. This suggests that the Seebeck coefficient for undoped Cu_3SbSe_4 decreases due to a rapidly increasing carrier concentration, caused by an intrinsic transition of undoped Cu_3SbSe_4 at temperatures above 523 K.

In contrast, the Seebeck coefficient for the Sn-doped specimens maintained a positive temperature dependence until 623 K, which suggests that intrinsic conduction may occur in Sn-doped specimens at temperatures above 623 K. As the Sn content increases, the Seebeck coefficient decreases because of the increased carrier concentration at constant temperature: 146–233 μVK^{-1} at 323–623 K for $Cu_3Sb_{0.98}Sn_{0.02}Se_4$, and 94–156 μVK^{-1} at 323–623 K for $Cu_3Sb_{0.92}Sn_{0.08}Se_4$. Yang et al. [5] reported a positive temperature dependence for Cu_3SbSe_4, with a Seebeck coefficient of 176–310 μVK^{-1} at 323–623 K. However, for $Cu_3Sb_{1-y}Sn_ySe_4$ (y = 0.025–0.05), the Seebeck coefficient decreased to 140–55 μVK^{-1} at 323 K and to 225–130 μVK^{-1} at 623 K. The decrease resulted from an increased carrier concentration from 7.5 × 10^{18} to 7.8 × 10^{19} cm^{-3}. Similarly, Wu et al. [11] reported a high Seebeck coefficient of 220–390 μVK^{-1} at 300–570 K for Cu_3SbSe_4, but the coefficient decreased to 175 μVK^{-1} at 300 K and 190 μVK^{-1} at 570 K for $Cu_3Sb_{0.98}Sn_{0.02}Se_4$. Furthermore, Wei et al. [15] found that for $Cu_3Sb_{1-y}Sn_ySe_4$ (y = 0.01–0.04), the increase in carrier concentration to 1.8 × 10^{20} cm^{-3} caused by Sn doping decreased the Seebeck coefficient from 160 to 90 μVK^{-1} at 323 K and from 250 to 160 μVK^{-1} at 623 K.

Figure 7 presents the power factor ($PF = \alpha^2\sigma$) for $Cu_3Sb_{1-y}Sn_ySe_4$. The PF influences the power output in thermoelectric power generation. The Seebeck coefficient

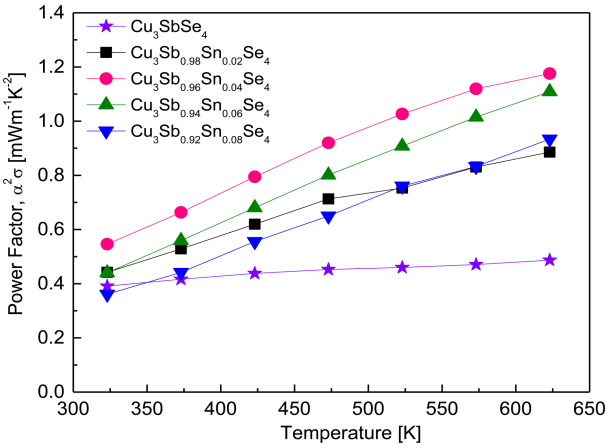

Fig. 7. Temperature dependence of the power factor of $Cu_3Sb_{1-y}Sn_ySe_4$.

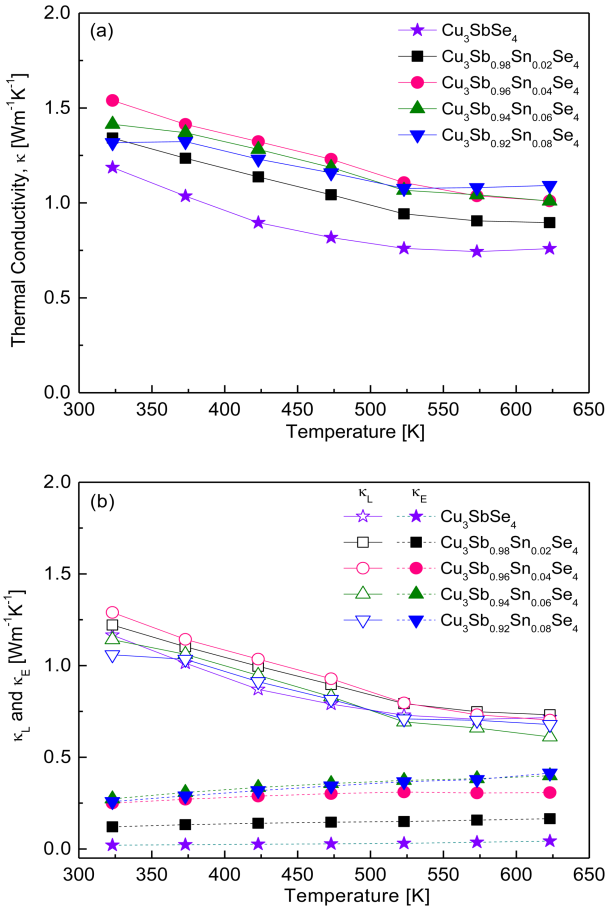

Fig. 8. Temperature dependence of the thermal conductivity of $Cu_3Sb_{1-y}Sn_ySe_4$: (a) total thermal conductivity and (b) lattice and electronic thermal conductivities.

and electrical conductivity are each affected differently by carrier concentration [21]. In this study, the *PF* increased with increasing temperature. The *PF* of Cu_3SbSe_4 was relatively low, at 0.39–0.49 mWm^{-1}K^{-2} at 323–623 K, with a low temperature dependence. However, as the Sn content increased, the *PF* and its temperature dependence rapidly increased, and thus the highest *PF* exhibited 0.55–1.18 mWm^{-1}K^{-2} at 323–623 K for $Cu_3Sb_{0.96}Sn_{0.04}S_4$. Similarly, Yang et al. [5] reported that the *PF* of Cu_3SbSe_4 was 0.15–0.50 mWm^{-1}K^{-2} at 300–673 K, and the *PF* was increased by Sn doping to 0.67–1.26 mWm^{-1}K^{-2} at 300–673 K for $Cu_3Sb_{0.975}Sn_{0.025}Se_4$ (the authors did not provide the *PF* in the literature, but it was calculated from the Seebeck coefficient and electrical conductivity). Wu et al. [11] reported that the *PF* of Cu_3SbSe_4 was low at 0.1–0.4 mWm^{-1}K^{-2} at 300–570 K, but that $Cu_3Sb_{0.98}Sn_{0.02}Se_4$ exhibited a higher *PF* of 0.8–1.3 mWm^{-1}K^{-2} at 300–570 K.

Figure 8 presents the thermal conductivity of $Cu_3Sb_{1-y}Sn_ySe_4$. As shown in Figure 8 (a), thermal conductivity tended to decrease with increasing temperature within our measured temperature range. Cu_3SbSe_4 had a thermal conductivity of 1.19–0.74 Wm^{-1}K^{-1} at 323–623 K, whereas Sn-doped samples exhibited higher conductivity values of 1.34–1.54 Wm^{-1}K^{-1} at 323 K and 0.90–1.09 Wm^{-1}K^{-1} at 623 K.

Thermal conductivity (κ) is calculated as follows: $\kappa = Dc_pd$, where (D) is thermal diffusivity, (c_p) is specific heat, and (d) is density. Therefore, thermal conductivity can be influenced by phase, composition, and microstructure (grain boundary, defect, and pore, among others) in accordance with various preparation processes. For example, Yang et al. [5] reported thermal conductivity of 2.3–1.0 Wm^{-1}K^{-1} at 323–623 K for $Cu_3Sn_ySb_{1-y}Se_4$ (y = 0.025–0.05) prepared by a melting-annealing process. Wu et al. [11] calculated a thermal conductivity of 1.25–0.91 Wm^{-1}K^{-1} at 300–570 K for $Cu_3Sb_{1-y}Sn_ySe_4$ (y = 0–0.02) synthesized by wet chemical reaction with organic precursors and HP method. Wei et al. [15] calculated a thermal conductivity of 3.60–1.30 Wm^{-1}K^{-1} at 300–673 K for $Cu_3Sn_ySb_{1-y}Se_4$ (y = 0.01–0.04) synthesized by MA and spark plasma sintering.

Compared with the above studies, the thermal conductivity in our samples, which were prepared by MA-HP, showed relatively low thermal conductivity values of 1.54–0.90 Wm^{-1}K^{-1} at 323–623 K for $Cu_3Sb_{1-y}Sn_ySe_4$ (y = 0.02–0.08).

Thermal conductivity consists of lattice thermal conductivity (κ_L) and electronic thermal conductivity (κ_E), which are determined by the contributions of phonons and carriers, respectively [22]. These two contributions can be separated by the Wiedemann–Franz law ($\kappa_E = L\sigma T$) as shown in Fig. 8 (b), where T is the absolute temperature and L is the temperature-dependent Lorenz number [5]. The lattice and electronic thermal conductivity exhibited negative and positive temperature dependence, respectively. For Cu_3SbSe_4, the lattice and electrical thermal conductivities were 1.17–0.72 and 0.02–0.04 $Wm^{-1}K^{-1}$ at 323–623 K, respectively. In contrast, the lattice thermal conductivity of the Sn-doped specimens decreased from 1.06–1.29 $Wm^{-1}K^{-1}$ at 323 K to 0.61–0.73 $Wm^{-1}K^{-1}$ at 623 K because of the enhanced phonon scattering caused by ionized impurities. However, the electronic thermal conductivity of the Sn-doped samples increased from 0.12–0.27 $Wm^{-1}K^{-1}$ at 323 K to 0.16–0.41 $Wm^{-1}K^{-1}$ at 623 K because of the increased carrier concentration generated by the doping. With the increase in Sn doping, the lattice thermal conductivity did not change significantly, whereas the electronic thermal conductivity increased. Therefore, although the total thermal conductivity of $Cu_3Sb_{1-y}Sn_ySe_4$ appears to be attributed mainly to its lattice thermal conductivity, the change in total thermal conductivity can be attributed mainly to its electronic thermal conductivity.

Figure 9 shows the temperature dependence of the Lorenz number for $Cu_3Sb_{1-y}Sn_ySe_4$. The Lorenz number ranges (1.45-2.44) × 10^{-8} V^2K^{-2}, with lower values indicating non-degenerate semiconducting behavior and higher values indicating degenerate semiconducting or metallic behavior [23]. The Lorenz number was estimated with the equation $L[10^{-8}V^2K^{-2}] = 1.5 + exp[-|\alpha|/116]$ [24]. The Lorenz number for Cu_3SbSe_4 was (1.57–1.56) × 10^{-8} V^2K^{-2} at 323–623 K, indicating non-degenerate semiconducting behavior. However, as the Sn content increased, the Lorenz number increased at constant temperature to (1.78–1.94) × 10^{-8} V^2K^{-2} at 323 K and to (1.63–1.76) × 10^{-8} V^2K^{-2} at 623 K. In comparison, Prasad et al. [14] reported the Lorenz number for $Cu_3Sb_{1-y}Sn_ySe_4$ (y = 0–0.04) was (1.57–1.89) × 10^{-8} V^2K^{-2} at 323 K.

Figure 10 presents the ZT for $Cu_3Sb_{1-y}Sn_ySe_4$, where $ZT = \alpha^2\sigma\kappa^{-1}T$. As can be observed, ZT increases with increasing

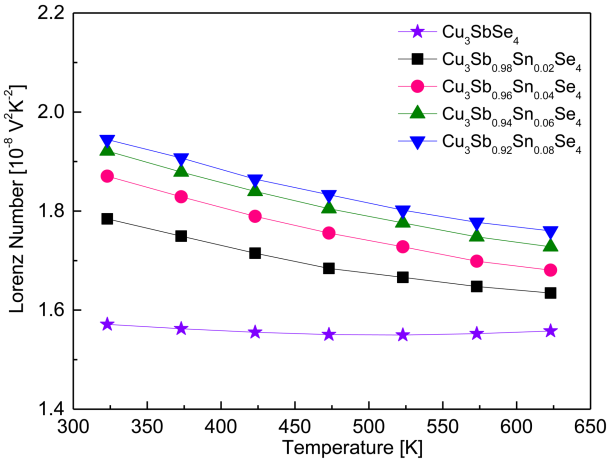

Fig. 9. Temperature dependence of the Lorenz numbers for $Cu_3Sb_{1-y}Sn_ySe_4$.

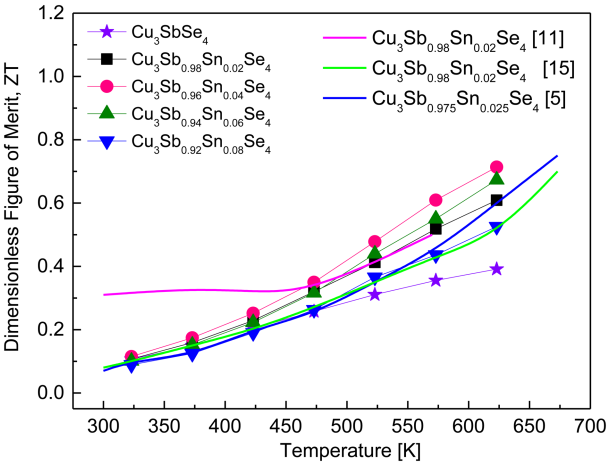

Fig. 10. Temperature dependence of the ZT values for $Cu_3Sb_{1-y}Sn_ySe_4$.

temperature, which is a result of the temperature dependences of the PF (Figure 7) and thermal conductivity (Figure 8). The ZT of $Cu_3Sb_{0.96}Sn_{0.04}Se_4$ was increased significantly by Sn doping (highest ZT of 0.71 at 623 K), compared with a ZT of 0.39 at 623 K for undoped Cu_3SbSe_4. This great increase was due to the remarkably improved PF, despite the increased thermal conductivity caused by Sn doping.

Yang et al. [5] reported a ZT of 0.04 for Cu_3SbSe_4 and a ZT of 0.75 $Cu_3Sb_{0.975}Sn_{0.025}Se_4$ at 673 K prepared by encapsulated melting and annealing method. Wu et al. [11] achieved a ZT of 0.24 for Cu_3SbSe_4 and a ZT of 0.48 for $Cu_3Sb_{0.98}Sn_{0.02}Se_4$ at 570 K synthesized by wet chemical reaction and HP

processes. Wei et al. [15] reported a *ZT* of 0.30 for Cu_3SbSe_4 and *ZT* of 0.69 for $Cu_3Sb_{0.98}Sn_{0.02}Se_4$ at 673 K, prepared by MA and spark plasma sintering. In this study, the MA-HP method used for solid-state synthesis was validated as an economical and practical process to save time and energy in preparing Sn-doped permingeatite compounds.

4. CONCLUSIONS

Herein, permingeatites $Cu_3Sb_{1-y}Sn_ySe_4$ (y = 0–0.08) were successfully prepared by employing an MA-HP process, and the thermoelectric properties of the permingeatites were examined at various levels of Sn doping. All the samples contained a single permingeatite phase of tetragonal structure without secondary phases. Undoped and Sn-doped samples exhibited p-type semiconductor behavior. Cu_3SbSe_4 exhibited non-degenerate semiconductor behavior, whereas Sn-doped samples transitioned to degenerate semiconductor behavior. As the Sn content increased, the *PF* was enhanced because of decreased Seebeck coefficient and increased electrical conductivity. However, thermal conductivity also increased with increasing electronic thermal conductivity, because of increased carrier concentration. Therefore, $Cu_3Sb_{0.96}Sn_{0.04}Se_4$ exhibited the highest *ZT* of 0.71 at 623 K because it had the highest PF (1.18 $mWm^{-1}K^{-2}$).

ACKNOWLEDGMENT

This study was supported by the Basic Science Research Capacity Enhancement Project (National Research Facilities and Equipment Center) through the Korea Basic Science Institute funded by the Ministry of Education (Grant No. 2019R1A6C1010047).

REFERENCES

1. K. Tyagi, B. Gahtori, S. Bathula, V. Toutam, S. Sharma, N. K. Singh, and A. Dhar, *Appl. Phys. Lett.* **105**, 261902 (2014).
2. A. Kumar, P. Dhama, and P. Banerji, *AIP Conf. Proc.* **1832**, 110050 (2016).
3. D. Zhang, J. Yang, Q. Jiang, Z. Zhou, X. Li, Y. Ren, J. Xin, A. Basit, X. He, W. Chu, and J. Hou, *J. Alloys Compd.* **724**, 597 (2017).
4. J. H. Pi, G. E. Lee, and I. H. Kim, *Korean J. Met. Mater.* **59**, 422 (2021).
5. C. Yang, F. Huang, L. Wu, and K. Xu, *J. Phys. D: Appl. Phys.* **44**, 295404 (2011).
6. E. Skoug, J. D. Cain, P. Majsztrik, M. Kirkham, E. L. Curzio, and D. T. Morelli, *Sci. Adv. Mater.* **3**, 602 (2011).
7. D. Zhao, D. Wu, and L. Bo, *Energies* **10**, 1524 (2017).
8. Y. Li, X. Qin, D. Li, X. Li, Y. Liu, J. Zhang, C. Song, and H. Xin, *RSC Adv.* **5**, 31399 (2015).
9. C. H. Chang, C. L. Chen, W. T. Chiu, and Y. Y. Chen, *Mater. Lett.* **186**, 227 (2017).
10. X. Y. Li, D. Li, H. X. Xin, J. Zhang, C. J. Song, and X. Y. Qin, *J. Alloys Compd.* **561**, 105 (2013).
11. Y. Wu, X. Qiao, X. Fan, X. Zhang, S. Cui S, and J. Wan, *J. Nanopart. Res.* **17**, 285 (2015).
12. D. Li, R. Li, X. Y. Qin, C. J. Song, H. X. Xin, L. Wang, J. Zhang, G. I. Guo, T. H. Zou, Y. F. Liu, and X. G. Zhu, *Dalton Trans.* **43**, 1888 (2014).
13. R. Bhardwaj, A. Bhattacharya, K. Tyagi, B. Gahtori, N. S. Chauhan, S. Bathula, S. Auluck, and A. Dhar, *Mater. Res. Bull.* **113**, 38 (2019).
14. K. S. Prasad and A. Rao, *J. Mater. Sci.: Mater. Electron.* **30**, 16596 (2019).
15. T. R. Wei, H. Wang, Z. M. Gibbs, C. F. Wu, G. J. Snyder, and J. F. Li, *J. Mater. Chem.* **2**, 13527 (2014).
16. G. E. Lee and I. H. Kim, *Materials* **14**, 1116 (2021).
17. J. W. Anthony, K. W. Bideaux, and M. C. Nichols, *Handbook of Mineralogy, Vol. 1: Elements, Sulfides, Sulfosalts* (Mineral Data Publishing, Tucson, Arizona, 2003) p. 1613.
18. H. Brooks, *Adv. Electron. Electron. Phys.* **7**, 85 (1955).
19. A. Suzumura, M. Watanabe, N. Nagasako, and A. Asahi, *J. Electron. Mater.* **43**, 2356 (2014).
20. A. Y. Eum, S. M. Choi, Y. S. Lim, W. S. Seo, J. S. Park, S. H. Yang, and I. H. Kim, *J. Korean Phys. Soc.* **66**, 1726 (2015).
21. D. Vashaee and A. Shakouri, *Phys. Rev. Lett.* **92**, 106103 (2004).
22. Y. Yan, H. Wu, G. Wang, X. Lu, and X. Zhou, *Energy Stor. Mater.* **13**, 127 (2018).
23. R. W. McKinney, P. Gorai, V. Stevanovic, and E. S. Toberer, *J. Mater. Chem. A* **5**, 17302 (2017).
24. B. Madavali and S. J. Hong, *J. Electron. Mater.* **45**, 6059 (2016).